JASA ARTICLE

# Direct numerical simulations of long-range infrasound propagation: Implications for source spectra estimation

Liam J. Tope,[1,2,a)] Jae Wook Kim,[1] and Peter Spence[2]
[1]Aerodynamics and Flight Mechanics Research Group, University of Southampton, Southampton SO17 1BJ, United Kingdom
[2]Atomic Weapons Establishment (AWE) plc., Reading, RG7 4PR, United Kingdom

**ABSTRACT:**
The evolution of observed dominant frequencies from a high-intensity infrasonic pulse with receiver range and stratospheric temperature is investigated using direct numerical simulations of the two-dimensional unsteady compressible Navier-Stokes equations. There is a high level of uncertainty in estimating source dominant frequencies based on received signals at sparse points on the ground. Nonlinear propagation effects in the ground-level thermospheric arrivals are found to significantly alter dominant frequency measurements compared to stratospheric arrivals with smaller amplitude sources. With a larger amplitude source, variations in observations are minimized as a result of nonlinear effects being ubiquitous across all atmospheric components of received signals but have a greater offset to the source dominant frequency. An approach to determine the source dominant frequency and minimize atmospheric variability is presented by calculating a source-to-receiver spectral transfer function averaged across the atmospheric states. This method reduces atmospheric variability in source frequency estimates within the pseudo-linear propagation regime and the average error to the known source frequency with a large amplitude source. The reduction of errors in source frequency estimates demonstrates the feasibility of using remote infrasound measurements as an indicator of source frequency and, in turn, the explosive yield of clandestine nuclear weapon test explosions.
 https://doi.org/10.1121/10.0024338
(Received 10 July 2023; revised 3 November 2023; accepted 14 December 2023; published online 22 January 2024)
[Editor: D. Keith Wilson] Pages: 465–478

## I. INTRODUCTION

The opening of the Comprehensive Nuclear-Test-Ban Treaty (CTBT) in 1996, along with its requirements for verification of compliance, has prompted the study of various explosive phenomena and their remote detection. Infrasound is a realistic candidate for such investigations because it can traverse hundreds to thousands of kilometers and be detected at ground level.[1] Consequently, a global infrasound detection network, the International Monitoring System (IMS), was established to support treaty verification and will comprise 60 detection array stations situated in 35 countries across the world on completion.[2]

Determining the origin of signals detected at these stations, as well as source properties, requires a comprehensive understanding of infrasound propagation through the atmosphere—numerical propagation modeling permits the use of investigations to develop this understanding. Low-fidelity modeling approaches prove an efficient method, although at the expense of the generality of the atmospheric state and acoustic field. Ray methods are a popular choice resulting from the ease of illustration of ray trajectories, however, the simplification of wave representation as ray paths instead of a continuous field neglects phenomena such as diffraction or scattering.[3] These effects require additional treatment, such as that used for propagation through caustics.[4] Restrictions, such as weakly range-dependent atmospheres[5] and no cross-winds[6] in modal-expansion-based models, also limit their functionality, whereas parabolic equation models, although perhaps the most versatile low-fidelity modeling approach with solutions developed for wide-angle propagation in three-dimensional (3D) inhomogeneous moving media,[7] still do not represent a complete description of infrasound propagation. Realistic acoustic field distortion in the atmosphere requires the inclusion of nonlinear propagation effects. Extensions have been made to existing low-fidelity modeling approaches to include weakly nonlinear effects,[8,9] and investigations of thermospheric infrasound arrivals at ground level in the finite-amplitude, geometrical limit have demonstrated a strong dependence between remote spectra and source overpressure, positing thermospheric infrasound as a reliable indicator of explosive yield.[10] Although these methods demonstrate promise for the efficient calculation of nonlinear atmospheric infrasound, it is also noted that more robust propagation models are needed for complete understanding of thermospheric infrasound.[10]

The requirement for nonlinear propagation modeling in the context of the detection of clandestine nuclear weapon test explosions is apparent within close vicinity to the source location, where source pressure amplitudes can be several orders of magnitude larger than the ambient pressure level.[11]

a)Email: L.J.Tope@soton.ac.uk

The exponential reduction of ambient atmospheric density with altitude also results in acoustic overpressure ratios in the thermosphere, which are several orders of magnitude larger than those at lower altitudes. Nonlinear propagation is, therefore, much more prevalent at such altitudes, resulting in signal steepening and lengthening.[12] *N*-wave formation along these propagation paths, followed by passage through caustics, has resulted in *U*-wave shaped signature observations at ground level.[13]

In recent years, there has been a progression toward the calculation of nonlinear infrasound propagation through direct numerical simulations (DNS) of the governing fluid dynamics equations. Such an approach allows for general fluids and source profiles, permitting investigations of the influence of more complex medium properties, including varying ground topography[14] and turbulent fields in the atmosphere.[15] Numerous studies have demonstrated these methods' feasibilities for observing propagation effects which low-fidelity models, thus far, have been unable to replicate, including nonlinear waveform distortion with different source strengths;[16] *N*-wave phase shifts through a thermospheric caustic;[17] and non-self-similar distortion of upward-propagating *N*-waves in the thermosphere.[18]

The dominant acoustic frequency can be used as an indicator of explosive yield[19] and is appealing over amplitude-based parameters because it is less sensitive to variations in atmospheric conditions, and frequency-dependent acoustic attenuation is relatively well understood.[20] Accordingly, in this work, DNSs of the two-dimensional Navier-Stokes equations are performed with the injection of a pulsed infrasonic source in realistic atmospheres, and observations of spectral transformations over range are made to ascertain uncertainties in different methods of determining the source dominant frequency. This aims to quantify uncertainties resulting from atmospheric and source conditions in methods based on averaging of these properties.

The paper is organized as follows. Section II outlines the governing equations and numerical methods used along with atmospheric and source specifications for the present simulations. Section III illustrates the variation of dominant frequencies of remotely detected signals with stratospheric temperatures and receiver ranges and introduces the approach used to minimize variations in these observations between different atmospheric states. Section IV uses observations of the full spectra of remote signals to calculate atmosphere-averaged source-to-receiver transfer functions, and the errors induced in dominant frequency approximations using these functions are determined. Last, Sec. V provides some concluding remarks.

## II. PROBLEM OUTLINE AND METHODOLOGY

The current problem of simulating the acoustic field generated by an explosive source in realistic atmospheric conditions using DNS techniques is illustrated in Fig. 1. This section describes the problem setup and computational methodologies used in this study.

### A. Computational domain and grid geometry

For the purposes of this study, the computational domain is a two-dimensional rectangular box of dimensions $(L_x, L_z)$ with a no-slip boundary condition along the boundary $(x, 0)$ to replicate the Earth's surface. All other domain boundaries are padded with an additional $L_s$ in which an artificial absorption "sponge-layer" is implemented to force the numerical solution to the ambient atmospheric condition and prevent spurious numerical reflections from their respective outer boundaries. DNS techniques are based on finite-differencing schemes and as such the computation domain is discretized into a regular grid. The grid points are uniformly spaced in much of the domain with the exception of increasing grid spacing in the sponge zones to further dissipate perturbations to ambient atmospheric state. Grid-stretching is also employed for large altitudes, $z > z_u$ km, because thermoviscous absorption contributes significantly more to acoustic field dissipation at thermospheric altitudes and with a strength proportional to the square of frequency,[20] precluding the necessity of fine grid spacings required at lower altitudes.

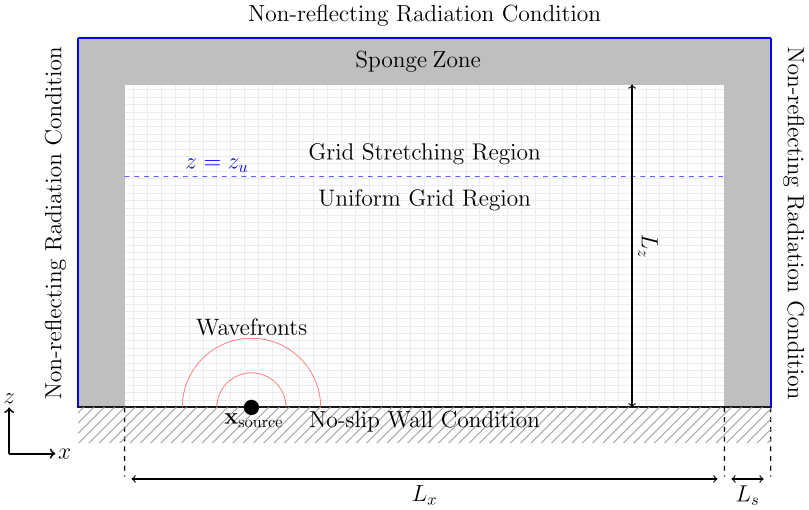


FIG. 1. (Color online) Sketch of the computational domain. The near-field region indicates where the grid spacing is uniform before grid-stretching is applied. The source is located directly above the origin, $\mathbf{x}_{\text{source}} = (0, z_{\text{source}})^T$. The source in the figure is displayed at $z_{\text{source}} = 0$ for diagrammatic purposes.

https://doi.org/10.1121/10.0024338

### B. Governing equations

To model the propagation of infrasound through the atmosphere, the two-dimensional compressible Navier-Stokes equations in a conservative form are used. These equations are transformed onto a generalized coordinate system, with source terms for the explosion and sponge-zone forcing previously discussed. Such a system of equations describes the evolution of the ambient atmospheric state further to acoustic perturbations. Numerical gradients of the ambient atmospheric condition must be highly resolved to retain numerical stability and, accordingly, these high-precision computations are avoided by subtracting the ambient hydrostatic equilibrium terms in the governing equations[16,17] such that

$$\frac{\partial}{\partial t}\left(\frac{\mathbf{Q}}{J}\right)+\frac{\partial}{\partial \xi_i}\left(\frac{\mathbf{E}'_j-\mathbf{E}'_{vj}}{J}\frac{\partial \xi_i}{\partial x_j}\right)+\frac{\mathbf{C}'}{J}=-\frac{\mathbf{S}_\sigma}{J}+\frac{\mathbf{S}}{J}. \quad (1)$$

Here, the indices, $i=1,2$ and $j=1,2$, denote the two dimensions, whereas the conservative variables and flux vectors are given by

$$\begin{aligned}\mathbf{Q}&=[\rho,\rho u,\rho v,\rho e_t]^T,\\ \mathbf{E}'&=\left[\rho u_j,\rho u u_j+\delta_{1j}p',\rho v u_j+\delta_{2j}p',(\rho e_t+p')u_j\right]^T,\\ \mathbf{E}'_v&=\left[0,\tau'_{1j},\tau'_{2j},u_i\tau'_{ji}+q'_j\right]^T,\end{aligned} \quad (2)$$

where the stress tensor and heat flux vector are written as

$$\begin{aligned}\tau'_{ij}&=\mu\left(\frac{\partial u'_i}{x_j}+\frac{\partial u'_j}{\partial x_i}-\frac{2}{3}\delta_{ij}\frac{\partial u'}{\partial x_i}\right),\\ q'_j&=\frac{\mu}{(\gamma-1)\mathrm{Pr}}\frac{\partial T'}{\partial x_j}\end{aligned} \quad (3)$$

for generalized coordinates $\xi_i=\{\xi,\zeta\}$, Cartesian coordinates $x_j=\{x,z\}$, Kronecker delta $\delta_{ij}$, $u_j=\{u,v\}$, $e_t=p/[(\gamma-1)\rho]+u_ju_j/2$, ratio of specific heat ratios $\gamma=1.4$ for air, and Prandtl number $\mathrm{Pr}=0.72$. The dynamic viscosity, $\mu$, is calculated using Sutherland's law.[21] The coordinate transformation from the Cartesian grid, $x_j$, to the generalized grid, $\xi_i$, has the Jacobian determinant $J^{-1}=|\partial(x,z)/\partial(\xi,\zeta)|$. The use of the perturbed fluid pressure $p'=p-p_0$, velocity $u'_j=u_j-u_{j0}$, and temperature $T'=T-T_0$ negates the requirement for accurate numerical modeling of the ambient hydrostatic equilibrium condition,

$$\frac{\mathrm{d}p_0}{\mathrm{d}z}=-\rho_0 g, \quad (4)$$

for gravitational acceleration, $g$, whilst also preventing time-evolution of the ambient state by neglecting diffusion of the ambient flow during acoustic propagation.[17] The corresponding buoyancy vector, $\mathbf{C}'$, is given by $\mathbf{C}'=[0,0,\rho' g,\rho' g v+p_0\nabla\cdot\mathbf{u}]^T$. Acoustic sources are included in the vector $\mathbf{S}$, and the additional source, $\mathbf{S}_\sigma$, is an artificial absorption term used to supplement the radiation boundary conditions.

### C. Numerical methods

Equation (1) is solved using high-order numerical schemes initially developed for application to aeroacoustic simulations. Flux derivatives are calculated using fourth-order pentadiagonal compact finite-difference schemes with a seven-point stencil[22] whilst numerical stability is sustained with sixth-order pentadiagonal compact filters with a cutoff wavenumber of $0.85\pi$ when normalized by the grid spacing.[23] These filters were determined to be sufficient in maintaining numerical stability and accuracy during nonlinear wave steepening for the present simulation parameters without additional artificial dissipation typically employed in the vicinity of shock fronts in DNS methods. Near and on the boundaries, polynomial-trigonometric blended extrapolation functions are used to devise noncentral compact schemes. Explicit time advancing of the solution is performed using a fourth-order Runge-Kutta scheme. The time step is determined by the smallest of the permissible time steps for a given Courant number, $C=c\Delta t/\Delta$, and Fourier number, $\mathrm{Fo}=\mu\Delta t/\Delta^2\rho$, for a given grid spacing, $\Delta$. Numerical stability of the ambient condition was found to be achieved with a Fourier number $\mathrm{Fo}=0.15$.

The boundary conditions used in the present study along the $x$- and $z$-directions are depicted in Fig. 1. The nonreflecting and no-slip wall boundary conditions are based on a quasi-linear characteristic wave equation.[24,25] A fixed temperature and zero fluid velocity condition are also used along the wall boundary at $z=0$. Sponge zones are employed to suppress outgoing disturbances before reaching the nonreflecting radiation boundary conditions. Disturbances near the nonreflecting boundaries are forced toward the ambient flow condition by the sponge-zone source term, $S_\sigma$, in Eq. (1).[26] This term is zero in the computation space and gradually increases to a maximum value, $\sigma_0=0.1$, at the boundary. Acoustic waves are attenuated and absorbed in the sponge-layer to prevent numerical reflections.

### D. Atmospheric state

Perhaps the largest subset of the parameter space that affects source-to-receiver transformations is that of the atmospheric state. To develop models for such transformations in atmospheres with various ducting characteristics, initially, simple atmospheric specifications are provided in the current work with the aim that additional complexity be added in future work to investigate the influence of additional physical effects on spectral transformations. To this end, eight different atmospheric states, $\Theta$, are considered to investigate the influence of stratospheric ducting strength on remote spectra characterization. All $\Theta$ are static over acoustic time scales and invariant with range such that $\Theta\equiv\Theta(z)$. A baseline temperature profile, $T_b$, is obtained by using the open-source climatological atmospheric model NRLMSISE-00.[27] This is an empirical model based on historical weather data, which, for given time and location specifications, outputs the relative composition and temperature of the

TABLE I. Input parameters used in NRLMSISE-00 model to generate the atmospheric profile used in the present study.

| Input parameter | Value |
|---|---|
| Year and day | 2013/1/14 |
| Time of day | 12:00 UTC |
| Geodetic latitude | 51.5074° |
| Longitude | −0.1278° |

atmosphere. To generate the atmosphere used for this study, the inputs given in Table I were used.

Additional space weather data required as inputs to the model can be found in Ref. 28. A perturbation is applied to the baseline temperature to generate a stratospheric maximum that is greater than or equal to the ground-level temperature to ensure refraction of the acoustic field toward the ground. This perturbation takes the form of a Gaussian function $T_{0i}(z) = T_b(z) + \delta T_i \exp\left[-4\ln(2)(z - z_{\text{ref}})^2/15^2\right]$, where the reference altitude, $z_{\text{ref}} = 47.7\,\text{km}$, is the altitude at which the stratospheric temperature peak occurs in $T_b(z)$, and $\delta T_i$ yield sound speed peaks in the stratosphere, $\delta c_{0i} = \{0, 1, 2, 4, 8, 16, 24, 32\}\,\text{m s}^{-1}$, for $\delta c_0 = \max_{z<100\,\text{km}}[c_0(z)] - c_0(z = 0)$. The maximum stratospheric temperature modeled in $T_{08}$ is $\sim 64\,^\circ\text{C}$, which is considerably warm for typical stratospheric temperatures but has been observed in extreme cases of sudden stratospheric warming (SSW).[29]

The atmospheric states are simply completed by computing the numerical integral of Eq. (4) with the ideal gas law, $\rho_{0i} = p_{0i}/RT_{0i}$, to obtain the ambient pressure and density for a ground-level pressure of 101 325 Pa. The atmospheres are considered stationary and, as such, no ambient winds, $\mathbf{u}_0 = [u_0, v_0]$, are imposed, therefore, $u_0(z) = v_0(z) = 0$. As previously stated, it is left as an outlook for future work that additional atmospheric complexity, such as temperature- and wind-induced ducting, be included in these simulations to further develop models for spectral transformations. These atmospheric states are denoted as $\Theta_i = \{T_{0i}, p_{0i}, \rho_{0i}, u_{0i}(z) = 0\ \forall\ z\}$. The sound speed profiles, $c_{0i}(z) = \sqrt{\gamma R T_{0i}(z)}$, are depicted in Fig. 2.

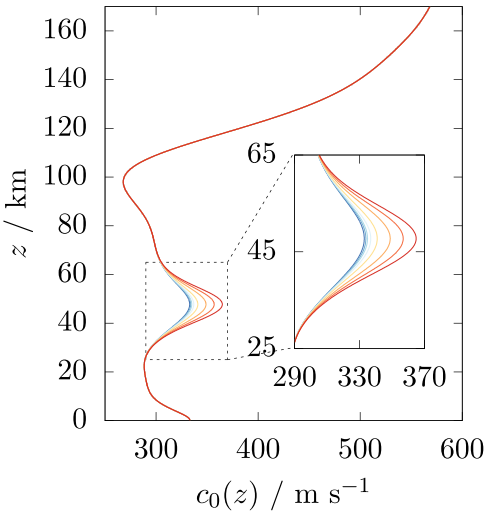


FIG. 2. (Color online) Speed of sound used for simulations of infrasound propagation through atmospheres of different stratospheric ducting strengths.

## E. Source definition

To replicate the rapid injection of large amounts of energy from explosive events, a forcing term is implemented in the energy equation $\mathbf{S} = [0, 0, 0, \mathcal{S}]^T$. The time-dependence of the source term is given by the derivative of a Gaussian pulse with half-width $t_{1/2}$ whilst the spatial distribution of the source is also prescribed by a Gaussian function with half-width $r_{1/2}$ such that

$$\mathcal{S}(\mathbf{x}, t) = \mathcal{A} \cdot -2b_t(t - t_0)e^{-b_t(t-t_0)^2} \cdot e^{-b_r r^2}, \tag{5}$$

for $r^2 = |\mathbf{x} - \mathbf{x}_{\text{source}}|^2$, $b_t = 4\ln(2)/t_{1/2}^2$, and $b_r = 4\ln(2)/r_{1/2}^2$. The parameter, $\mathcal{A}$, is used to prescribe the source strength and expressed in units of source pressure amplitude, Pa. This particular source model is similar to those previously used in the literature and was chosen because of its N-like pressure signature at the source location.[17] Indeed, atmospheric signal properties from such a source model have been well documented.[16–18] Two source amplitudes are used, $\mathcal{A} = 10^3$ Pa and $\mathcal{A} = 10^4$ Pa, as it was found that nonlinear effects were observed in stratospheric arrivals for $\mathcal{A} = 10^4$ Pa but not for $\mathcal{A} = 10^3$ Pa. This allows the present work to quantify the influence of nonlinear effects on source characterization. The spatial half-width of the source is set to $r_{1/2} = 1$ km, and the time width of the pulse is set to $t_{1/2} = 1$ s. The pulse onset time is given by $t_0 = 3t_{1/2}$, and the source location is set to an airburst of $\mathbf{x}_{\text{source}} = [0, 1.5]$ km. Both sources, therefore, have the same dominant frequency, $f_D = \{f \,|\, S_{\Phi\Phi}(f) = \max_{f'} S_{\Phi\Phi}(f')\}$, hence, any observed variations in the remote signals between the two sources are caused by amplitude differences alone. Using this source profile yields a time signature and power spectral density (PSD) at ground level below the source displayed in Fig. 3.

## F. Numerical details

A domain of size $\mathcal{D}_{\text{physical}} = \{x \in [-150, 615]\,\text{km}, z \in [0, 170]\,\text{km}\}$, where sponge zones of size $L_s = 30$ km appended as depicted in Fig. 1, is used. The computational domain is discretized using $N_x = 12\,800$, $N_z = 2800$ grid points. As a result of the large increase in thermoviscous absorption at thermospheric altitudes,[20] grid-stretching is employed from $z > z_u = 130$ km such that dampened high frequencies are not unnecessarily resolved. This results in grid spacing, $\Delta = \Delta x = \Delta z = 62$ m, in the uniform-grid region, $\mathcal{D}_{\text{uniform}} = \{x \in [-150, 615]\,\text{km}, z \in [0, 130\,\text{km}\}$. The grid spacing at $z = 170$ km, immediately before more aggressive sponge-zone grid-stretching, is $\Delta \approx 100$ m. For the present source parameters, this corresponds to a minimum of ∼37.8 points-per-wavelength at the source dominant frequency, $f_D = 0.14$ Hz, in $\mathcal{D}_{\text{uniform}}$ and ∼ 55 points-per-wavelength for the same frequency at 170 km due to the difference in sound speed, $c_0(z)$, at each altitude. The

https://doi.org/10.1121/10.0024338

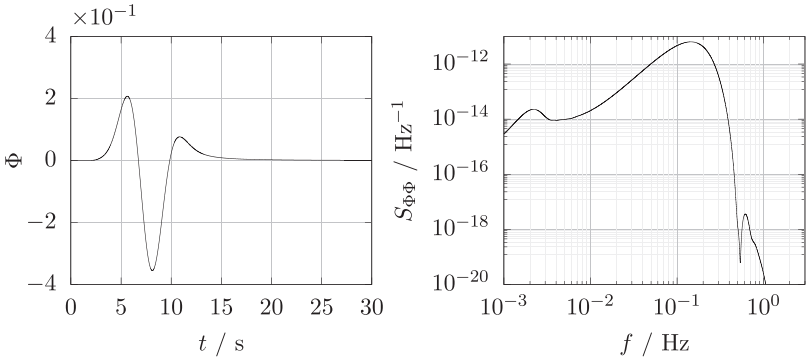


FIG. 3. Normalized pressure waveform, $\Phi = p'\sqrt{\rho_0(z_{\text{source}})}/\mathcal{A}\sqrt{\rho_0(0)}$, and PSD, $S_{\Phi\Phi}$, of the $\mathcal{A} = 10^3$ Pa signal detected at ground level below the source location.

maximum frequency resolved using eight points-per-wavelength is 0.54 Hz in $\mathcal{D}_{\text{uniform}}$ and 0.68 Hz at 170 km altitude. The time step determined by the Fourier number is more restrictive at thermospheric altitudes than at the Courant number, which with the present grid parameters results in $\Delta t \sim 4 \times 10^{-3}$ s.

The ambient density of the atmosphere generally decreases exponentially with altitude such that at above ∼160 km, the density is on the order of 9 orders of magnitude smaller than at ground level. At such altitudes, the overpressure ratio of acoustic perturbations to the ambient condition is likely to be much larger than that at lower altitudes. To reduce the relative amplitude of the acoustic perturbations and, thus, complement the radiation boundary condition at high altitudes, the ambient pressure and density within the sponge zone is artificially increased by slowly reducing the gravitational strength from $g$ to $-g$.[16] Further, inside the sponge region, $z > L_z$, the viscosity is artificially reduced via an exponential decay function such that the small densities and large viscosities do not affect the time step imposed by the Fourier condition.

The computation is parallelized via domain decomposition and message passing interface (MPI) approaches. The calculation of numerical fluxes and filtering requires the inversion of the pentadiagonal coefficient matrices. A parallelization approach based on quasi-disjoint matrix systems[30] is used to avoid numerical artifacts at subdomain boundaries. This method has been shown to provide superlinear scalability with the number of cores/subdomains used. With 1280 processor cores on the University of Southampton IRIDIS supercomputing cluster, this resulted in a run-time of ∼13 h per case.

## III. VARIATIONS IN REMOTE SPECTRA WITH STRATOSPHERIC TEMPERATURES

### A. Characterization of the acoustic field

Acoustic amplitudes scale proportionally with the square of the exponentially decaying ambient density.[31] Accordingly, the acoustic pressure field is scaled by the source amplitude, $\mathcal{A}$, and $\sqrt{\rho_0}$ such that

$$\Phi(\mathbf{x},t) = \frac{p(\mathbf{x},t) - p_0(\mathbf{x})}{\mathcal{A}} \sqrt{\frac{\rho_0(\mathbf{x}_{\text{source}})}{\rho_0(\mathbf{x})}}. \tag{6}$$

For frequency-domain analyses, the PSD is calculated. Before frequency-domain transformations are made, the zero-frequency component is removed through

$$\Phi_a(\mathbf{x},t) = \Phi(\mathbf{x},t) - \bar{\Phi}(\mathbf{x}), \tag{7}$$

where $\bar{\Phi}(\mathbf{x})$ denotes the time-averaged normalized pressure. The one-sided PSD of the pressure fluctuations is then calculated by[32]

$$S_{\Phi\Phi}(\mathrm{x},f) = \lim_{T\to\infty} \frac{\hat{\Phi}_a(\mathbf{x},f,T)\hat{\Phi}_a^*(\mathbf{x},f,T)}{T}, \tag{8}$$

where $\hat{\Phi}_a$ denotes a discrete Fourier transform approximation of the continuous transformation,

$$\hat{\Phi}_a(\mathbf{x},f,T) = \int_{-T}^{T} \Phi(\mathbf{x},t) e^{-2\pi i f t} \mathrm{d}t, \tag{9}$$

and "*" denotes the complex conjugate.

To suppress numerical artifacts in the frequency-domain transformation and subsequently calculated transfer functions, piecewise-averaging of the power spectra, $S_{\Phi\Phi}$, is employed,

$$S^i_{\Phi\Phi} = \sum_{j=-n+1}^{n} \frac{S^{i-j-1}_{\Phi\Phi} + S^{i+j}_{\Phi\Phi}}{2n}, \tag{10}$$

where $S^i_{\Phi\Phi} = S_{\Phi\Phi}(f^i)$ and a uniform frequency spacing, $f^{i+1} - f^i = \Delta f \ \forall\ i$, is assumed. Persisting numerical oscillations in the power spectra are filtered out by using cubic spline interpolation with the numerical peaks as knot locations in frequency ranges where numerical oscillations are prevalent. Boundary conditions that match the derivative of the spline functions to the original spectra gradient in adjacent frequency ranges where numerical peaks are absent are used to maintain a continuous interpolated function.

### B. Description of the acoustic field

The acoustic field initially propagates uniformly in space, where waves detected on the ground are solely from direct source-to-receiver propagation paths along the ground, $\Phi_G$. Temperature gradients rapidly distort the acoustic field from its initial spherical distribution. Negative

temperature gradients in the troposphere result in upward refraction of the acoustic field, whereas positive temperature gradients in the stratosphere induce refraction back toward ground level. These stratospheric refractions are subsequently observed on the ground and denoted $\Phi_S$. Reflections of $\Phi_S$ from the Earth's surface, $\Phi_{S_2}$, are observed on the ground at larger ranges via the same refraction mechanisms. Acoustic energy, which has not been ducted within the Earth-stratosphere waveguide, continues to propagate upward before refracting back toward the ground because of large positive temperature gradients in the thermosphere. This thermospheric refraction, $\Phi_T$, typically has a zone of audibility, where it can be detected at ground level, between those of $\Phi_S$ and $\Phi_{S_2}$. The ranges and time of arrival of these different signal components at ground level vary significantly between each atmosphere due to varying ducting strengths. As a representation of the acoustic field development, snapshots of the acoustic field within the atmosphere $\Theta_2(z)$ are depicted in Fig. 4.

Atmospheres with varying ducting strengths not only yield remote signals with different arrival times and audibility zones for atmospheric refractions, but the magnitude of these signal components varies also. Figure 5 depicts the scaled pressure at retarded time, $\tau = t - x/c_0(z=0)$, as a function of range for the atmospheres with the smallest and largest stratospheric temperatures, $\Theta_1(z)$ and $\Theta_8(z)$, respectively.

The differences in magnitude of the atmospheric components as a function of stratospheric temperatures is intuitive as larger stratospheric temperatures cause a greater proportion of the acoustic energy spectrum to be contained within the Earth-stratosphere waveguide. However, the consequence of stratospheric temperature variations on dominant frequencies observed at ground level, labeled $f_D$, is not immediately clear *a priori*. Figure 5 demonstrates that for low-temperature stratospheres, thermospheric magnitudes are significant between overlapping audibility zones for the stratospheric components $\Phi_S$ and $\Phi_{S_2}$. Contrastingly, in high-temperature stratospheres, the overlapping stratospheric audibility zones contain stratospheric components of magnitudes that are significantly larger than the thermospheric component. The dominant frequencies of the composite signal are, therefore, subject to a large degree of variation at any given range for different atmospheric conditions. Furthermore, the functional dependence of $f_D(x)$ adds an additional degree of variation between atmospheric conditions. Therefore, remote observations of dominant infrasonic frequencies are likely to be largely variable between different atmospheric conditions.

### C. Variation of remote dominant frequency

To quantify the uncertainties in yield calculations from observations of remote dominant frequencies, it is necessary to ascertain the magnitude of discrepancies in $f_D$ from different atmospheric conditions. Figure 6 presents the observed

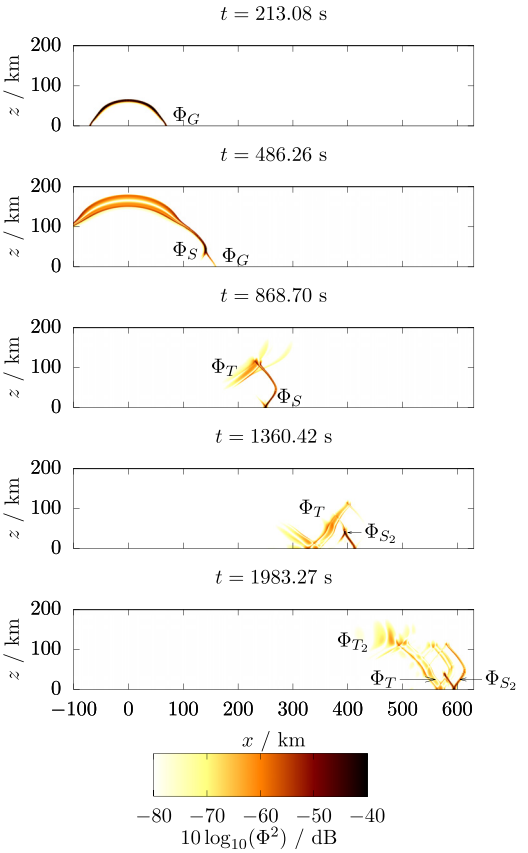


FIG. 4. (Color online) Logarithm of the normalized acoustic pressure in the physical domain at different simulation times. The stratospheric refractions, $\Phi_S$ and $\Phi_{S_2}$, and thermospheric refraction, $\Phi_T$, are observed at ground level for the given ranges and simulation times.

$f_D$ for the atmospheres $\Theta_1(z)$ and $\Theta_8(z)$ and peak source magnitudes $\mathcal{A} = 10^3$ and $\mathcal{A} = 10^4$ Pa.

Figure 6 demonstrates that atmospheres of different stratospheric ducting strength give rise to remote signals which vary in dominant frequency and its gradient with the receiver range as a result of different onset ranges of the audibility zone and the maximum return height of waves bound within the Earth-stratospheric waveguide. $\Theta_1(z)$ yields lower dominant frequencies observed at range than the warmer stratospheric case $\Theta_8(z)$, whereas the rate of change of these observed frequencies with range is similarly smaller for lower stratospheric temperatures. Differences in the functional variation of $f_D(x)$ between the two atmospheres can be interpreted by the proportion of energy bound within the waveguide for different propagation paths. However, the prominence of purely stratospheric arrivals at ground level for the warmer stratosphere reduces the influence of nonlinear propagation and thermoviscous absorption, maintaining a consistent frequency band for each stratospheric arrival. With weaker stratospheric ducting, the thermospheric component contributes to the dominant frequency within stratospheric shadow zones. For $\Theta_1(z)$, this is within the range 400–500 km, where the observed dominant frequency is much lower than at other ranges, as a result of signal lengthening from nonlinear propagation and high-frequency absorption within the thermosphere.

https://doi.org/10.1121/10.0024338

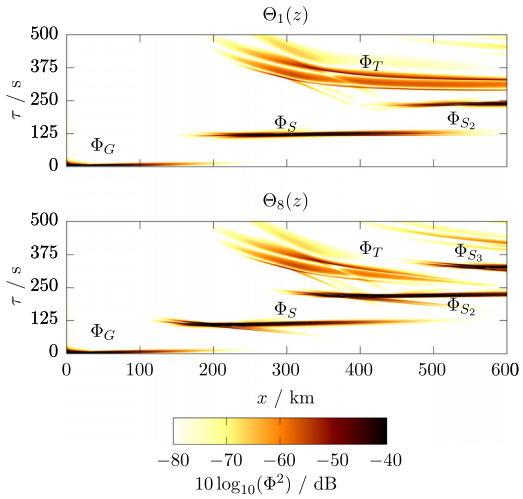


FIG. 5. (Color online) Logarithm of the normalized acoustic pressure observed at ground level at a range $x$ with retarded time $\tau = t - x/c_0(z = 0)$ from propagation in atmospheres $\Theta_1(z)$ and $\Theta_8(z)$.

With the larger source amplitude, the dominant frequency and its rate of change with receiver range are reduced relative to the smaller source amplitude. This is most apparent for the stratospheric arrivals. Accordingly, remote dominant frequencies observed in atmosphere $\Theta_8(z)$ from peak source amplitudes $\mathcal{A} = 10^3$ and $\mathcal{A} = 10^4$ Pa differ consistently for all ranges where atmospheric refractions are observed. Contrastingly, $\Theta_1(z)$ yields discrepancies between observed frequencies for the two source amplitudes at ranges where the stratospheric components are dominant, but at 400–500 km range where the thermospheric arrival dominates, nonlinear propagation effects are observed for both sources, yielding an approximately equal dominant frequency. The observed frequency from the thermospheric component is also more comparable to those from the stratospheric components with a peak source magnitude of $\mathcal{A} = 10^4$ Pa, reducing the variability of $f_D$ with range further to the reduced rate of change within stratospheric audibility zones.

### D. Normalized receiver range

The variation in observed dominant frequencies between different atmospheres is largely influenced by the differing geometrical structure of the acoustic field. To minimize these discrepancies with the aim of using remote frequency measurements as a reliable indicator of source frequency, the range is normalized by the nearest remote receiver of an atmospheric arrival. Using two-dimensional ray-tracing,[33] the nearest receiver of an atmospheric arrival for a given ray inclination angle $\theta$, $x_n(\theta)$, was determined by the range of the first minimum of the ray trajectory, $z(x)$. The nearest receiver distance is then the minimum value of the function $x_n(\theta)$, $x_{\text{nearest}} = \min_\theta x_n(\theta)$. The receiver distance functions, $x_n(\theta)$, calculated for each atmosphere, $\Theta_i$, are depicted in Fig. 7.

The effect of reducing variability between remote signals from different atmospheric conditions by comparing results at normalized ranges, $x^* = x/x_{\text{nearest}}$, is demonstrated by the ray paths given in Fig. 8.

In Fig. 8, the atmospheres with the smallest and largest stratospheric temperatures, $\Theta_1$ and $\Theta_8$, respectively, are shown to exhibit greatly different ranges, $x$, of stratospheric arrivals. In particular, the first atmospheric arrival in $\Theta_1$ occurs within a partial shadow zone between subsequent atmospheric arrivals in $\Theta_8$. Comparing signals at ranges, $x$, between these two atmospheres is clearly problematic. Using the normalized range approach, therefore, allows for comparisons between atmospheres where there are common refraction-induced atmospheric arrivals.

The geometrical acoustic method used to generate $x_n(\theta)$ does not account for diffraction and, thus, yields larger predicted $x_{\text{nearest}}$ than those observed from the simulation signals. This effect would be most clear in atmospheres with no stratospheric ducting predicted by ray models, yet, where stratospheric diffraction is observed.[17] In the present results, the atmosphere, $\Theta_1(z)$, has a predicted $x_{\text{nearest}} = 281$ km by the ray model, whereas the –60 dB contour in Fig. 5 indicates that the diffracted wavefront is prominent in magnitude from a range ~190 km. Despite this, the approximate range from the ray method is a more accurate indicator of the geometrical structure of the acoustic field because integer values of $x^*$ correspond to successive observed bounces of the stratospheric component, as depicted in Fig. 8. This cyclical behavior of successive observations is not immediately clear in the diffracted arrivals observed in Fig. 5. Although the geometrical structure of ray paths between different atmospheres still varies over $x^*$, the retention of common composite signals from atmospheric refractions for different $\Theta_i$ is expected to minimize atmospheric variability to a much larger degree. Figure 9 depicts the range of

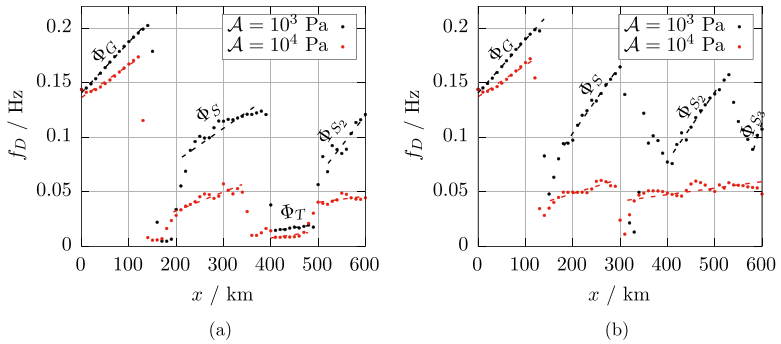


FIG. 6. (Color online) Dominant frequency, $f_D$, of signals detected with range $x$ for propagation through atmospheres (a) $\Theta_1(z)$ and (b) $\Theta_8(z)$. Data points are taken from ranges at intervals of 10 km. The dashed lines represent a linear fit of $f_D(x)$ to demonstrate the effective range of the dominant signal components, which are labeled accordingly.

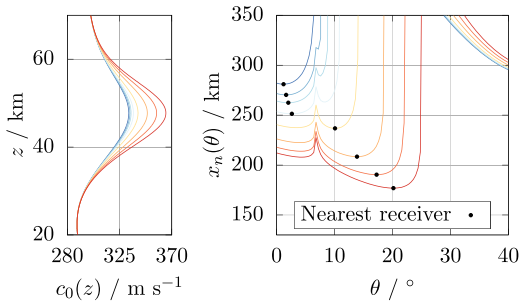


FIG. 7. (Color online) Ray receiver distance with inclination angle with overall nearest receiver $x_{\text{nearest}}$ for each atmosphere $\Theta_i$.

discrepancies in the remote dominant frequencies to the source value, $\delta f_D = f_{D_{\text{receiver}}} - f_{D_{\text{source}}}$, for all atmospheres for normalized ranges, $x^* \in [1, 2]$.

As indicated in the comparisons of the observed dominant frequencies in atmospheres $\Theta_1(z)$ and $\Theta_8(z)$, depicted in Fig. 6, the largest source amplitude yields a much larger difference to the source dominant frequency, averaging at $\sim$0.1 Hz (77%), but the variations across different atmospheric conditions and receiver ranges are significantly smaller. In contrast, for approximately linear propagation, where $\mathcal{A} = 10^3$ Pa, the average errors at ranges near the onset of the stratospheric audibility zones are much smaller, averaging at $\sim$0.029 Hz (20%) for $1 < x^* < 1.4$ but have a large degree of variation between atmospheres. This is particularly noted at ranges where the $\Phi_S$ audibility zone diminishes, and thermospheric components influence the observed spectra. Whilst the influence of nonlinear propagation clearly inhibits the efficacy of using remote dominant frequencies to approximate the source value, the minimal variation between different atmospheric conditions, especially at the onset of the audibility zones, suggests that suitable corrections to remote observations could be made for a general atmosphere to improve the estimate of the source dominant frequency at range. By way of an example, the average offset in source-to-receiver $f_D$—depicted by the lines and points in Fig. 9—is subtracted from the observed dominant frequency to obtain a refined estimate of the source, $f_D$. This is shown in Fig. 10.

## IV. APPROXIMATIONS OF REMOTE SPECTRAL TRANSFORMATIONS

Section III demonstrated that using remote spectral properties to approximate those of the source can yield uncertainties from atmospheric variability, nonlinear propagation, and receiver range. This section aims to, instead, investigate the transformation of the entire infrasound spectrum due to passage through the atmosphere and whether a general transfer function based on averaged atmospheric conditions can yield accurate approximations for the source dominant frequency, where reduced variability is the result of the atmospheric state.

### A. Characterization of power spectra transformations

To investigate the feasibility of estimating the source dominant frequency from remote spectra for a range of atmospheric conditions, first, it is necessary to develop a model for the forward transformation of the spectral components—from the source to the receiver. Such a model can then be used to inform the choice of the inverse transformation and, in turn, the source spectra. A transfer function, $\mathcal{H}$, with a simple inverse is, therefore, considered as follows:

$$\begin{aligned} S_{\Phi\Phi}(x,f) &= \mathcal{H}(S_{\Phi\Phi}(x_{\text{source}},f)) \\ &= \Psi(x,f,\Theta) S_{\Phi\Phi}(x_{\text{source}},f)), \end{aligned} \tag{11}$$

such that $\Psi$ is determined by the remote spectra normalized by the source spectra. Likewise, once a model for the transfer function, $\Psi(x,f,\Theta)$, has been determined, the inverse can be used to approximate the source spectra,

$$S_{\Phi\Phi}(x_{\text{source}},f) = \Psi(x,f,\Theta)^{-1} S_{\Phi\Phi}(x,f). \tag{12}$$

In the calculation of the transfer functions, the source spectra are approximated by the spectra at ground level, 1.5 km below the source center.

### B. Transfer functions at normalized range

Transfer functions for normalized receiver ranges, $x^* = \{1, 1.5, 2\}$, are depicted in Figs. 11–13 for source magnitudes $\mathcal{A} = 10^3$ and $\mathcal{A} = 10^4$ Pa.

At the normalized range, $x^* = 1$, each atmosphere yields the first stratospheric arrival at ground level. The transfer functions at this range are, therefore, dominated by the $\Phi_S$ component as the ground component, $\Phi_G$, is severely attenuated and thermospheric arrivals are not detected. Despite the variation in ray paths of the stratospheric refractions observed at this range from different atmospheric conditions, discrepancies between transfer functions within the frequency band 0.02–0.1 Hz are minimal for both source

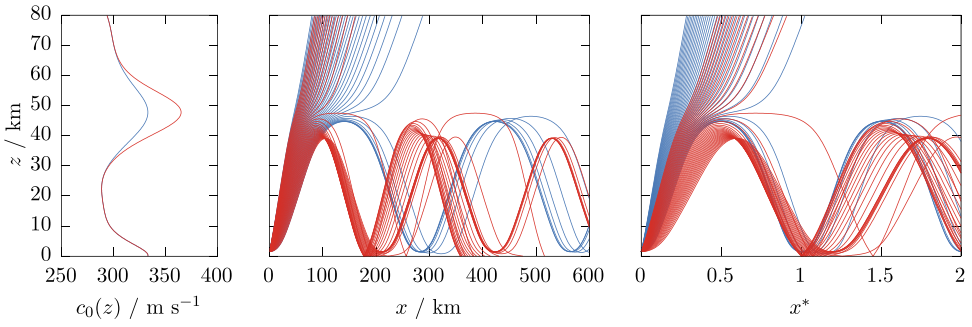


FIG. 8. (Color online) Ray paths from atmospheres $\Theta_1$ and $\Theta_8$ with physical ranges $x$ and normalized ranges $x^*$.

https://doi.org/10.1121/10.0024338

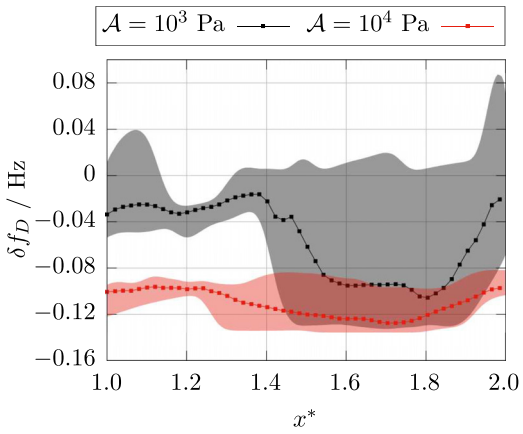


FIG. 9. (Color online) Measured offset between the remote and source dominant frequency with normalized range. The lines and points indicate the average difference to the source, $f_D$, for all atmospheres whilst the bounds of the corresponding shaded regions indicate the minimum and maximum differences observed.

amplitudes. Deviations seem to occur where prominent features of the transfer functions appear. First, for smaller stratospheric atmospheric sound speeds, an increase in $\Psi$ is observed at $f \approx 0.01$ Hz but is less pronounced for increasing stratospheric ducting strengths. Second, the spectra at $f \approx 0.2$ Hz is attenuated more heavily than at other frequencies, in particular, when nonlinear propagation effects cause spectral shifts from signal lengthening and steepening. The strength of this attenuation varies by up to 2 orders of magnitude between the atmospheres $\Theta_1(z)$ and $\Theta_8(z)$ with a peak source magnitude of $\mathcal{A} = 10^3$ Pa. Last, the increase in magnitude at frequencies $f > 0.3$ Hz results vary between atmospheres with stronger stratospheric ducting yielding greater amplification of these spectral components. At $f = 1$ Hz, differences in $\Psi$ between $\Theta_1$ and $\Theta_8$ are as great as 4 orders of magnitude for $\mathcal{A} = 10^3$ Pa. Discrepancies between different atmospheres are similarly observed in this frequency range for $\mathcal{A} = 10^4$ Pa, although at $f = 1$ Hz, the maximum difference observed is ∼2 orders of magnitude between $\Theta_1(z)$ and $\Theta_8(z)$.

Within the partial shadow zone between the arrival $\Phi_S$ and $\Phi_{S_2}$, it is expected that there is greater variability between different atmospheres as was observed in Sec. III for the dominant frequency. This is due to the greater variation of stratospheric arrival paths at these ranges as well as the prominence of the thermospheric component. Increased deviations in $\Psi$ for different $\Theta$ at $x^* = 1.5$ with respect to those at $x^* = 1$ are observed in Fig. 12.

Discrepancies in $\Psi(\Theta)$ within the frequency band 0.02–0.1 Hz increase by an order of magnitude for both values of $\mathcal{A}$ displayed compared to the minimal differences observed at $x^* = 1$, whereas at the frequency extrema, discrepancies are more comparable. The atmosphere $\Theta_8$ yields larger spectral strengths within this frequency band whilst atmospheres with weaker stratospheric ducting display greater attenuation. As demonstrated in Fig. 5, at range $x^* = 1.5$, the atmosphere $\Theta_8$ is dominated by stratospheric components, whereas for $\Theta_1$, thermospheric components are of comparable magnitude to $\Phi_S$ and $\Phi_{S_2}$, thus, heavily affecting the transfer function. The larger propensity for nonlinear propagation and absorption at thermospheric altitudes compared to stratospheric altitudes, therefore, appears to induce these increased discrepancies.

At $x^* = 2$, the stratospheric component again dominates the remote signals for all atmospheres, and, hence, comparisons of transfer functions are more appropriate. The transfer functions at this range are depicted in Fig. 13.

At these ranges, for $\mathcal{A} = 10^3$ Pa, the difference in magnitude between the local $\Psi$ maxima at $f \approx 0.02$ Hz and minima at $f \approx 0.1$ Hz is larger than that observed at $x^* = 1$. For the atmospheres with largest amount of stratospheric ducting, the local $\Psi$ maxima at $f \approx 0.02$ Hz is indeed larger at this range despite increased losses associated with the greater path lengths traversed. This is attributed to greater influence of nonlinear propagation effects in $\Phi_{S_2}$ compared

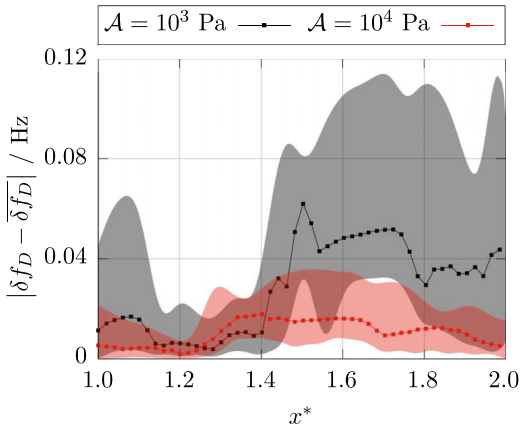


FIG. 10. (Color online) Magnitude of difference between the remote dominant frequency after removing the mean offset with range to the known value and the source dominant frequency with normalized range. The lines and points indicate the average difference to the source, $f_D$, across all atmospheres whilst the bounds of the corresponding shaded regions indicate the minimum and maximum differences observed.

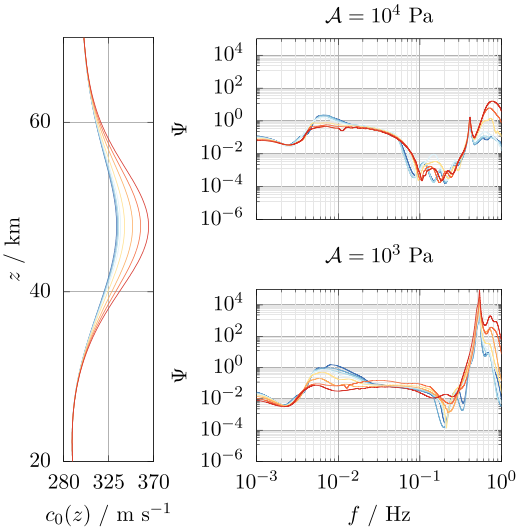


FIG. 11. (Color online) Transfer functions for all atmospheres $\Theta_i$ at normalized range $x^* = 1$.

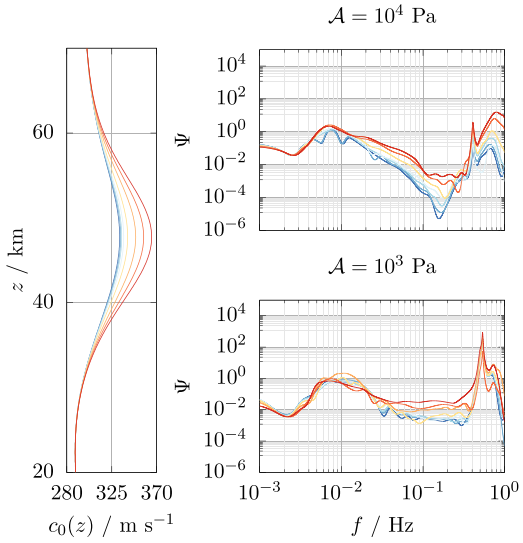


FIG. 12. (Color online) Transfer functions for all atmospheres $\Theta_i$ at normalized range $x^* = 1.5$.

to $\Phi_S$. This is likely to be a result of increased exposure to higher altitudes with lower ambient pressures. Additionally, the increased influence of nonlinear effects in $\Psi_{S_2}$ results in similar transfer function magnitudes around the dominant source frequency for the two source magnitudes. Despite this, the high-frequency attenuation with $\mathcal{A} = 10^4$ Pa is still much more pronounced. Differences between the various $\Theta(z)$ are smaller compared to those observed at $x^* = 1.5$ for the majority of the frequency band. The previously defined $\Psi$ maxima and minima retain similar differences in magnitude for each $\Theta$, but at intermediate frequencies, differences are minimal.

### C. Discussion of results

The present transfer function comparisons at normalized ranges indicate that the current approach to minimize uncertainties due to atmospheric variability is sufficient at near-integer values of $x^*$ for much of the infrasound frequency band. Despite this, prominent features of the transfer functions at frequencies $f \approx 0.01$, $f \approx 0.2$, and $f > 0.3$ Hz deviate in magnitude by a factor of up to 100. Of these spectral properties, which differ between each $\Theta(z)$, the largest frequencies presented have a greater chance of numerical error affecting the results. The maximum frequency that can be adequately resolved using four points-per-wavelength within the Earth-stratosphere waveguide is $f \approx 1$ Hz, correspondingly, a frequency of $f \approx 0.5$ Hz can be resolved with eight points-per-wavelength. The present numerical simulations are, therefore, band limited to a tolerable error up to 0.5 Hz, whereas larger frequencies are likely to be subject to numerical dissipation and dispersion. Furthermore, the source PSD magnitude at $f = 0.5$ Hz is of the same order as machine precision, $\mathcal{O}(10^{-16})$. This further presents limitations in obtaining a physical understanding of the results at larger frequencies as numerical uncertainties from finite-differencing schemes are compounded by limitations in numerical precision in the subsequent analyses in the frequency domain.

Despite this, the atmospheric response to high-intensity pulsed acoustic sources is evident in the transfer functions calculated from the present simulations. Atmospheres with larger stratospheric sound speeds cause greater proportion of the acoustic energy to be bound within the Earth-stratosphere waveguide. Consequently, the remotely detected signals at all ranges are composed of signals dominated by the stratospheric component and have a greater total magnitude. This is observed in the results in Sec. IV B, as the integrals of the transfer functions for atmospheres $\Theta_8(z)$ and $\Theta_7(z)$ are visibly larger than their counterparts with $\Theta_1(z)$, for example. At ranges where the stratospheric component is the only detected atmospheric refraction, e.g., $x^* = 1$, higher frequencies are enhanced relative to the source spectra, whereas in contrast, low frequencies are diminished, albeit to a lesser degree. This effect is more prominent for larger stratospheric temperatures and, thus, stronger stratospheric ducting. The influence of waveform steepening and signal lengthening with $\mathcal{A} = 10^4$ Pa is also evident for all $\Theta_i(z)$ with decreased transfer function magnitudes in the 0.3–1 Hz band. The effect of nonlinear wave propagation is observed most significantly where the stratospheric refractions are the largest in magnitude, which is the result of larger acoustic pressures maintained along stratosphere-ducted paths and less energy leakage into the thermosphere. Accordingly, greater increases in $\Psi$ in the low-frequency band 0.005–0.02 Hz between the two source magnitudes considered are observed for the atmospheres with larger peak sound speeds in the stratosphere. Similarly, a greater decrease in relative signal strength around the source dominant frequency is observed. Consequently, at this range, where stratospheric ducting alone produces the remote spectra, nonlinear propagation appears to reduce uncertainties due to atmospheric variability. Similar effects are observed at the second stratospheric receiver locations

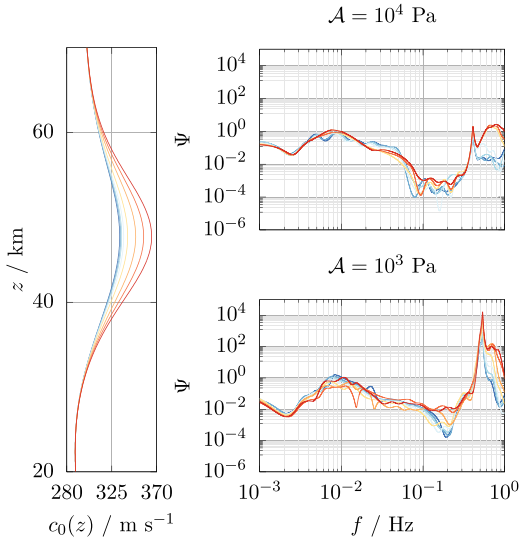


FIG. 13. (Color online) Transfer functions for all atmospheres $\Theta_i$ at normalized range $x^* = 2$.

https://doi.org/10.1121/10.0024338

$x^* = 2$. This is potentially beneficial for generating general empirical transfer functions that can be used to approximate source spectra from remote detection of large amplitude explosions.

The combination of thermospheric and stratospheric ducting at larger ranges induces an increase in low-frequency strength for high-temperature stratospheres such that transfer function variability caused by atmospheric conditions is reduced in the 0.005–0.02 Hz band. In stratospheric shadow zones, however, a generic empirical transfer function from an average of atmospheric conditions would likely yield large uncertainties due to the variation of transfer function magnitudes at larger frequencies. Dominant frequencies of purely thermospheric arrivals similarly induce a large error in approximating the source dominant frequency as a result of nonlinear propagation and thermoviscous absorption. The errors induced by atmospheric variability in approximating general transfer functions compared to simply approximating the source dominant frequency by that which is observed at the receiver are discussed in greater detail in Sec. IV D.

### D. Errors in source frequency approximations

As observed from the results in Sec. IV C, generating a general empirical transfer function for the purpose of approximating the source dominant frequency in a general atmosphere will induce errors as a result of atmospheric variability and source magnitude. Here, the magnitude of this error is calculated and compared against the errors associated with using the remote dominant frequency alone as a measure of the present method's feasibility for source characterization and, therefore, CTBT verification.

To measure the likelihood of inducing errors from atmospheric variability, we can define an averaged transfer function,

$$\langle \Psi \rangle_\Theta(x,f) = \frac{1}{N}\sum_i^N \Psi_{\Theta_i}(x,f), \tag{13}$$

which is subsequently used to approximate the source spectra,

$$\tilde{S}_{00}|_{\Theta_i,x} = S_{\Phi\Phi}|_{\Theta_i}(x,f)/\langle \Psi \rangle_\Theta(x,f), \tag{14}$$

for each atmosphere $\Theta_i(z)$, $i = [1,8]$ and range. An estimate for the source dominant frequency is then made using the approximate source spectra. The absolute error in the approximated dominant frequency, $\tilde{f}_D$, is then evaluated using $\delta f_D = f_D - \tilde{f}_D$. These errors for each atmosphere and source amplitude are depicted in Fig. 14. For each source amplitude case, the averaged transfer function was determined using its corresponding remote spectra.

As observed from the transfer functions in Fig. 12, at ranges within the stratospheric shadow zone, $x^* = 1.5$, atmospheric variability is significantly increased and results in larger averaged errors in $\tilde{f}_D$. Within these ranges, errors are

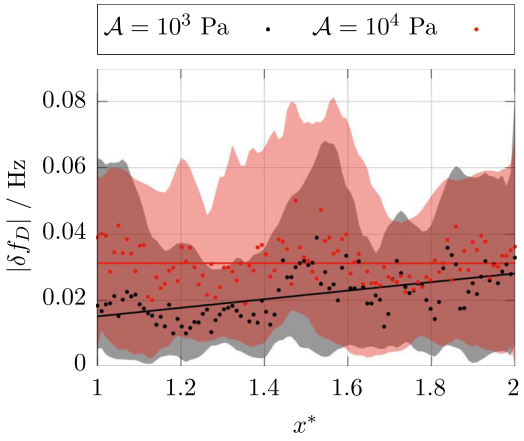


FIG. 14. (Color online) Errors in dominant frequency due to atmospheric variability for both source amplitudes. The points indicate the averaged error across all atmospheres, the corresponding shaded region depicts the range of errors, and the solid lines depict the linear fit of the averaged errors.

on the order of 0.04 Hz for $\mathcal{A} = 10^3$ Pa and 0.05 Hz for $\mathcal{A} = 10^4$ Pa, corresponding to ∼27% and 35% error, respectively. Despite the increase in errors at these ranges, they are a significant improvement on the errors presented in Fig. 9 for the same range. The average error in Fig. 9 using $\tilde{f}_D = f_D(x)$ for $\mathcal{A} = 10^3$ Pa peaked at ∼69% compared to 27% when using an averaged transfer function. Similarly, the average error is smaller near-integer values of $x^*$ from ∼29% to ∼14% at $x^* = 1$ and $\mathcal{A} = 10^3$ Pa. Despite this, there is an increase in the range of errors observed at $x^* = 1$ compared to the previous method. Near $x^* = 1$, it may, therefore, be more suitable to use the previous approach to approximate the source dominant frequency for certain atmospheric conditions which deviate greatly from the present averaged atmosphere. Last, at $x^* = 2$, the average and maximum error

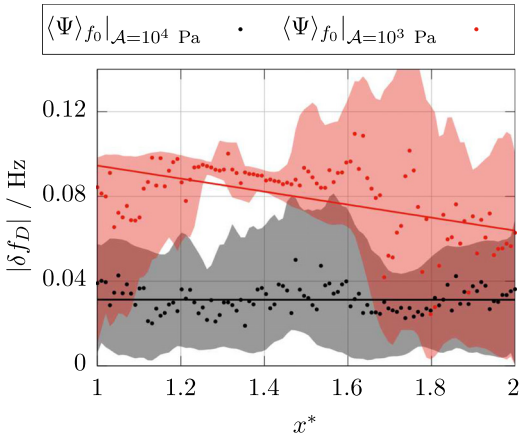


FIG. 15. (Color online) Errors in dominant frequency due to source amplitude variation. The points indicate the averaged error across each atmosphere, the corresponding shaded region depicts the range of errors from different atmospheres, and the solid lines depict the linear fit of the averaged errors. The black points result from approximating the $\mathcal{A} = 10^4$ Pa source spectra with an averaged transfer function from $\mathcal{A} = 10^4$ Pa data, whereas the red points used an averaged transfer function from $\mathcal{A} = 10^3$ Pa data.

in the dominant frequency from the present approach are also reduced with respect to the previous method.

The previous method demonstrated that nonlinear propagation induced a shift toward lower dominant frequencies in remote signals. As a result, discrepancies to the source dominant frequency were large compared to the pseudo-linear case. The present method yields a significant decrease in error for the dominant frequency; however, this is obvious because the remotely detected signals for $\mathcal{A} = 10^4$ Pa were used to inform the choice of its respective transfer function. To demonstrate the influence of variability in source parameters in generating general empirical transfer functions, the remote spectra from $\mathcal{A} = 10^3$ Pa were instead used to construct the averaged transfer function and approximate the source spectra from remote signals with $\mathcal{A} = 10^4$ Pa. The resulting errors in approximate dominant frequency are displayed in Fig. 15.

Using the remote signals from the weaker source to generate the transfer function yields a significant increase in approximated dominant frequency from remote spectra with $\mathcal{A} = 10^4$ Pa. For much of the normalized range, errors are over twice as large as those induced by atmospheric variability alone. This error begins to decrease as the receiver range increases, however, as observed in Fig. 13, the $\Phi_{S_2}$ component seemingly exhibits greater nonlinear propagation effects compared to $\Phi_S$, thus, there is reduced error in using $\mathcal{A} = 10^3$ Pa to approximate $\Psi$. This demonstrates the significance of nonlinear propagation in influencing remote spectra and, therefore, the importance of capturing its effects in propagation modeling.

## V. CONCLUDING REMARKS

DNSs of the two-dimensional unsteady compressible Navier-Stokes equations have been performed, and observations of the dominant frequency of remotely detected signals have been observed. Efforts to minimize the uncertainty of these observations were made in an attempt to obtain consistent estimates for the source dominant frequency between different atmospheric conditions. The dominant frequency was shown to vary significantly across different atmospheres resulting from variations in the geometrical structure of the acoustic field as well as the proportion of energy bound within the Earth-stratosphere waveguide. Nonlinear propagation and thermoviscous absorption in the ground-level thermospheric arrivals also significantly alters dominant frequency measurements with smaller amplitude sources, whereas with a larger amplitude source, variations in these observations are minimized because nonlinear signal lengthening and steepening are ubiquitous across all atmospheric components of the received signals.

Due to large discrepancies in the receiver dominant frequency with large infrasonic sources and significant uncertainties induced by atmospheric variability, a second approach to determining the source dominant frequency was presented by calculating a source-to-receiver spectral transfer function averaged across the atmospheric states. This approach was found to reduce atmospheric variability in source frequency estimates within the pseudo-linear propagation regime and the average error to the known source frequency with a large amplitude source. The importance of capturing nonlinear propagation in numerical modeling is also highlighted by the increased errors in dominant frequency estimates using small source amplitude data for large source amplitude observations. The results of this work demonstrate the feasibility of obtaining source frequency estimates such as those to inform on the accuracy and uncertainty of explosive yield approximations.

## ACKNOWLEDGMENTS

This research was co-funded by the Atomic Weapons Establishment (AWE) and the Engineering and Physical Sciences Research Council (EPSRC) via Centre for Doctoral Training in Next Generation Computational Modelling (CDT-NGCM, Grant No. EP/L015382/1). The authors gratefully acknowledge the computing facilities and services of the IRIDIS 5 High Performance Computing cluster at the University of Southampton.

## AUTHOR DECLARATIONS

### Conflict of Interest

The authors have no conflicts to disclose.

## DATA AVAILABILITY

The data that support the findings of this study are available from the corresponding author upon reasonable request.

## APPENDIX: VALIDATION OF THERMOSPHERIC GRID-STRETCHING

Section II highlighted the restrictive nature of the Fourier condition on the stable time step for the simulation of infrasound through thermospheric altitudes. Citing the increased atmospheric absorption of high frequencies at such altitudes, it was suggested that the computation grid be stretched above a threshold altitude, $z_u$, to vastly increase the permissible time step without resolving negligible high frequencies. This appendix provides validation of this approach through comparisons of thermospheric acoustic pressures between a uniform grid and one which employs thermospheric grid-stretching.

### 1. Domain setup

A truncated computational domain is considered with a minimal extent in $x$ such that purely positive-$z$ propagation can be investigated. This domain is defined as $\mathcal{D}_{\text{minimal}} = \{x \in [-10, 10]\,\text{km}, z \in [0, 170]\,\text{km}\}$, with sponge zones of length $L_{\sigma x} = 10$ and $L_{\sigma z} = 30$ km appended as demonstrated in Fig. 1. The stretched grid uses $N_x = 500$, $N_z = 2800$ points, and increases the $\Delta z$ spacing at altitude $z > z_u = 130$ km. At lower altitudes, the vertical grid spacing is

https://doi.org/10.1121/10.0024338

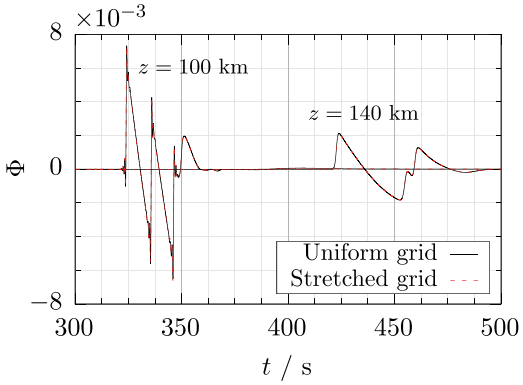


FIG. 16. (Color online) Normalized acoustic pressures at altitudes 100 and 140 km directly above the source for a uniform reference grid and one which employs thermospheric grid-stretching, respectively.

uniform and has a value of $\Delta z \approx 62$ m. At 170 km altitude, prior to the sponge zone, the stretched grid has a grid spacing of $\Delta z \approx 100$ m. The uniform grid is formed of $N_x = 500$, $N_z = 3800$ grid points with a smaller spacing of $\Delta z \approx 52$ m in the entirety of the physical domain and used to generate reference solutions for the acoustic pressures. Simulations of infrasound propagation from a $\mathcal{A} = 10^3$ Pa source described in Eq. (5) were run in each case in the atmosphere $\Theta_1$ up to a time of ~680 s. The atmosphere $\Theta_1$ was chosen because of to its low stratospheric temperature, permitting greater acoustic energy leakage into the thermosphere than other atmospheres presently considered. Furthermore, the source amplitude $\mathcal{A} = 10^3$ was used in favor of $\mathcal{A} = 10^4$ Pa as waves entering the thermosphere are of higher frequency due to negligible nonlinear lengthening following passage through the stratosphere. As a result, this source model will provide a more robust numerical benchmark than its larger source amplitude counterpart. All other numerical implementation details are consistent with those described in Sec. II.

## 2. Results

Normalized acoustic pressures between each grid case are given in Fig. 16.

At 100 km, the normalized acoustic pressure exhibits an $N$-wave shape indicative of nonlinear steepening as a result of low thermospheric densities. In fact, two overlapping $N$-waves are observed as a result of the source's offset from the ground as the first and second $N$-waves originate from the initially upward-propagating waves and the reflection of initially downward propagating waves. At this altitude, both grids are uniform and the waveforms exhibit minimal differences. At 140 km, within the grid-stretching region, the waveform has lengthened as a result of nonlinear propagation such that the interfering $N$-waves construct a smoother composite signal. Despite the increase in grid spacing, the waveform from the stretched grid is still in agreement with the reference uniform grid.

A quantitative assessment of the applicability of the stretched thermospheric grid approach was performed by evaluating the error in acoustic pressure to that predicted by the reference grid. This error is given by

$$\varepsilon = \frac{1}{\max_t\{p'_u, p'_s\}} \sqrt{\frac{1}{N}\sum_{i=1}^{N}\left(p'_{si} - p'_{ui}\right)^2} \tag{A1}$$

for a discrete-time $t_i$, $i \in [1, N]$. This error was evaluated at 1 km altitude intervals directly above the source. The resulting altitude variations in error with the grid spacing alongside for reference is given in Fig. 17.

The results demonstrate that despite the grid-stretching employed, errors to the reference grid do not increase in the applicable region $z > z_u$. Therefore, the use of such grid-stretching does not decrease the numerical accuracy of the calculated acoustic field for the present application and can be used to prevent large computational load increases caused by extending the maximum altitude of these simulations into the thermosphere.

[1]E. W. Carpenter, G. Harwood, and T. Whiteside, "Microbarograph records from the Russian large nuclear explosions," Nature **192**(4805), 857 (1961).
[2]J. Marty, "The IMS infrasound network: Current status and technological developments," in *Infrasound Monitoring for Atmospheric Studies: Challenges in Middle Atmosphere Dynamics and Societal Benefits*, edited by A. Le Pichon, E. Blanc, and A. Hauchecorne (Springer International Publishing, Cham, 2019), pp. 3–62.
[3]P. Blom and R. Waxler, "Modeling and observations of an elevated, moving infrasonic source: Eigenray methods," J. Acoust. Soc. Am. **141**(4), 2681–2692 (2017).
[4]R. Sabatini, C. Bailly, O. Marsden, and O. Gainville, "Characterization of absorption and non-linear effects in infrasound propagation using an augmented Burgers' equation," Geophys. J. Int. **207**(3), 1432–1445 (2016).
[5]M. Bertin, C. Millet, and D. Bouche, "A low-order reduced model for the long range propagation of infrasounds in the atmosphere," J. Acoust. Soc. Am. **136**(1), 37–52 (2014).

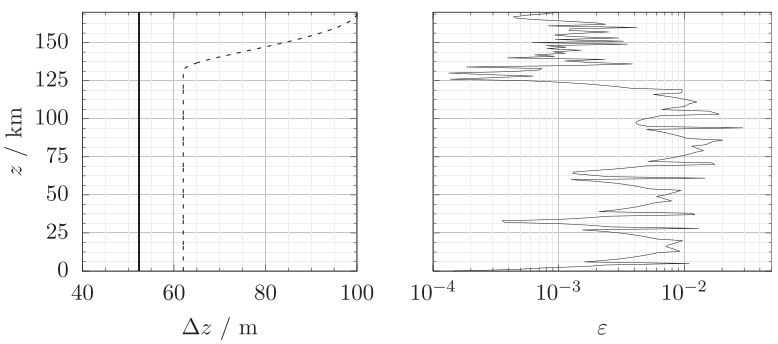


FIG. 17. Grid spacing of the uniform and stretched grids and the observed errors in the acoustic pressure.

[6]J. Assink, R. Waxler, and D. Velea, "A wide-angle high Mach number modal expansion for infrasound propagation," J. Acoust. Soc. Am. **141**(3), 1781–1792 (2017).
[7]J. F. Lingevitch, M. D. Collins, D. K. Dacol, D. P. Drob, J. C. W. Rogers, and W. L. Siegmann, "A wide angle and high Mach number parabolic equation," J. Acoust. Soc. Am. **111**(2), 729–734 (2002).
[8]J. B. Lonzaga, R. M. Waxler, J. D. Assink, and C. L. Talmadge, "Modelling waveforms of infrasound arrivals from impulsive sources using weakly non-linear ray theory," Geophys. J. Int. **200**(3), 1347–1361 (2015).
[9]J. Scott, P. Blanc-Benon, and O. Gainville, "Weakly nonlinear propagation of small-wavelength, impulsive acoustic waves in a general atmosphere," Wave Motion **72**, 41–61 (2017).
[10]P. Blom and R. Waxler, "Characteristics of thermospheric infrasound predicted using ray tracing and weakly non-linear waveform analyses," J. Acoust. Soc. Am. **149**(5), 3174–3188 (2021).
[11]G. F. Kinney and K. J. Graham, *Explosive Shocks in Air* (Springer Science and Business Media, Berlin, 2013).
[12]M. F. Hamilton and D. T. Blackstock, *Nonlinear Acoustics* (Academic, San Diego, 1998), Vol. 237.
[13]R. Marchiano, F. Coulouvrat, and J.-L. Thomas, "Nonlinear focusing of acoustic shock waves at a caustic cusp," J. Acoust. Soc. Am. **117**(2), 566–577 (2005).
[14]C. D. de Groot-Hedlin, "Infrasound propagation in tropospheric ducts and acoustic shadow zones," J. Acoust. Soc. Am. **142**(4), 1816–1827 (2017).
[15]R. Sabatini, J. B. Snively, C. Bailly, M. P. Hickey, and J. L. Garrison, "Numerical modeling of the propagation of infrasonic acoustic waves through the turbulent field generated by the breaking of mountain gravity waves," Geophys. Res. Lett. **46**(10), 5526–5534, https://doi.org/10.1029/2019GL082456 (2019).
[16]O. Marsden, C. Bogey, and C. Bailly, "A study of infrasound propagation based on high-order finite difference solutions of the Navier-Stokes equations," J. Acoust. Soc. Am. **135**(3), 1083–1095 (2014).
[17]R. Sabatini, O. Marsden, C. Bailly, and C. Bogey, "A numerical study of nonlinear infrasound propagation in a windy atmosphere," J. Acoust. Soc. Am. **140**(1), 641–656 (2016).
[18]R. Sabatini, O. Marsden, C. Bailly, and O. Gainville, "Three-dimensional direct numerical simulation of infrasound propagation in the Earth's atmosphere," J. Fluid Mech. **859**, 754–789 (2019).
[19]P. Golden, P. Negraru, and J. Howard, "Infrasound studies for yield estimation of HE explosions," TR-2012-0084, Southern Methodist University, Dallas, TX (2012).
[20]L. C. Sutherland and H. E. Bass, "Atmospheric absorption in the atmosphere up to 160 km," J. Acoust. Soc. Am. **115**(3), 1012–1032 (2004).
[21]F. M. White, *Viscous Fluid Flow* (McGraw-Hill, New York, 1991), Vol. 3.
[22]J. W. Kim, "Optimised boundary compact finite difference schemes for computational aeroacoustics," J. Comput. Phys. **225**(1), 995–1019 (2007).
[23]J. W. Kim, "High-order compact filters with variable cut-off wavenumber and stable boundary treatment," Comput. Fluids **39**(7), 1168–1182 (2010).
[24]J. W. Kim and D. J. Lee, "Generalized characteristic boundary conditions for computational aeroacoustics," AIAA J. **38**(11), 2040–2049 (2000).
[25]J. W. Kim and D. J. Lee, "Generalized characteristic boundary conditions for computational aeroacoustics, Part 2," AIAA J. **42**(1), 47–55 (2004).
[26]J. W. Kim, A. S. Lau, and N. D. Sandham, "Proposed boundary conditions for gust-airfoil interaction noise," AIAA J. **48**(11), 2705–2710 (2010).
[27]J. M. Picone, A. E. Hedin, D. P. Drob, and A. C. Aikin, "NRLMSISE-00 empirical model of the atmosphere: Statistical comparisons and scientific issues," J. Geophys. Res. **107**(A12), SIA 15-1–SIA 15-16, https://doi.org/10.1029/2002JA009430 (2002).
[28]"CelesTrak space weather data," available at https://celestrak.org/SpaceData/ (Last viewed November 2019).
[29]P. Braesicke and U. Langematz, "On the occurrence and evolution of extremely high temperatures at the polar winter stratopause—A GCM study," Geophys. Res. Lett. **27**(10), 1467–1470, https://doi.org/10.1029/2000GL011431 (2000).
[30]J. W. Kim, "Quasi-disjoint pentadiagonal matrix systems for the parallelization of compact finite-difference schemes and filters," J. Comput. Phys. **241**, 168–194 (2013).
[31]C. de Groot–Hedlin, "Finite-difference time-domain synthesis of infrasound propagation through an absorbing atmosphere," J. Acoust. Soc. Am. **124**(3), 1430–1441 (2008).
[32]M. E. Goldstein, *Aeroacoustics* (McGraw-Hill, New York, 1976).
[33]P. Blom and R. Waxler, "Impulse propagation in the nocturnal boundary layer: Analysis of the geometric component," J. Acoust. Soc. Am. **131**(5), 3680–3690 (2012).